AGU PUBLICATIONS

JGR

Journal of Geophysical Research: Oceans

RESEARCH ARTICLE

10.1002/2016JC012256

Key Points:
- 3-D structure for coherent mesoscale eddies in the North Atlantic subtropical gyre
- Transient transport of heat and salt
- Role of mesoscale eddies in shaping the SSS maximum

Supporting Information:
- Supporting Information S1

Correspondence to:
A. Amores
amores@hawaii.edu

Citation:
Amores, A., O. Melnichenko, and N. Maximenko (2017), Coherent mesoscale eddies in the North Atlantic subtropical gyre: 3-D structure and transport with application to the salinity maximum, *J. Geophys. Res. Oceans*, *122*, 23–41, doi:10.1002/2016JC012256.

Received 18 AUG 2016
Accepted 30 NOV 2016
Accepted article online 20 DEC 2016
Published online 5 JAN 2017

Coherent mesoscale eddies in the North Atlantic subtropical gyre: 3-D structure and transport with application to the salinity maximum

Angel Amores [1], Oleg Melnichenko [1], and Nikolai Maximenko [1]

[1]International Pacific Research Center, SOEST, University of Hawaii, Honolulu, Hawaii, USA

Abstract The mean vertical structure and transport properties of mesoscale eddies are investigated in the North Atlantic subtropical gyre by combining historical records of Argo temperature/salinity profiles and satellite sea level anomaly data in the framework of the eddy tracking technique. The study area is characterized by a low eddy kinetic energy and sea surface salinity maximum. Although eddies have a relatively weak signal at surface (amplitudes around 3–7 cm), the eddy composites reveal a clear deep signal that penetrates down to at least 1200 m depth. The analysis also reveals that the vertical structure of the eddy composites is strongly affected by the background stratification. The horizontal patterns of temperature/salinity anomalies can be reconstructed by a linear combination of a monopole, related to the elevation/depression of the isopycnals in the eddy core, and a dipole, associated with the horizontal advection of the background gradient by the eddy rotation. A common feature of all the eddy composites reconstructed is the phase coherence between the eddy temperature/salinity and velocity anomalies in the upper ∼300 m layer, resulting in the transient eddy transports of heat and salt. As an application, a box model of the near-surface layer is used to estimate the role of mesoscale eddies in maintaining a quasi-steady state distribution of salinity in the North Atlantic subtropical salinity maximum. The results show that mesoscale eddies are able to provide between 4 and 21% of the salt flux out of the area required to compensate for the local excess of evaporation over precipitation.

1. Introduction

Mesoscale eddies are ubiquitous features in ocean circulation [*Chelton et al*., 2007, 2011] that play an important role in the redistribution of heat and salt throughout the ocean [*Wunsch*, 1999; *Roemmich and Gilson*, 2001; *Hausmann and Czaja*, 2012]. Despite their importance, the time-mean eddy heat and salt fluxes remain poorly characterized, mainly due to difficulties in gathering observations on mesoscale time and space scales. Most studies represent only limited geographic regions where adequate observations exist [*Amores et al*., 2013; *Roemmich and Gilson*, 2001], or rely on the outputs of ocean general circulation models [*Tréguier et al*., 2014; *Jayne and Marotzke*, 2002]. Ocean models, however, may have their own biases and uncertainties, arising from misrepresented physics, limited resolution (both vertical and horizontal) and/or errors in boundary conditions, among other factors [*Jayne and Marotzke*, 2002]. Thus, direct estimates of the eddy fluxes from observations are much needed in order to create a consistent description.

Using model outputs can be avoided if one takes advantage of the ensemble of Argo profile data collected over the past decade that, combined with the use of high spatial and temporal resolution of satellite data, allows the reconstruction of a three-dimensional (3-D) structure of a mean eddy in a given area [*Chaigneau et al*., 2011]. This idea has been successfully used to study mesoscale structures in areas with high eddy kinetic energy such as the Agulhas rings [*Souza et al*., 2011], mesoscale eddies in the eastern South Pacific [*Chaigneau et al*., 2011], South Atlantic Bight and the Gulf Stream Recirculation [*Castelao*, 2014], and the Antarctic Circumpolar Current [*Frenger et al*., 2015]. However, to the best of our knowledge, it has not been used before for areas of low eddy kinetic energy such as in the interior of a subtropical gyre.

In this study, we focus on the reconstruction of the 3-D eddy structure and its induced heat and salt transient transport in the North Atlantic subtropical gyre, a region characterized by a relatively low eddy kinetic energy (EKE) level (Figure 1), where eddy heat and salt transports are traditionally considered to have a

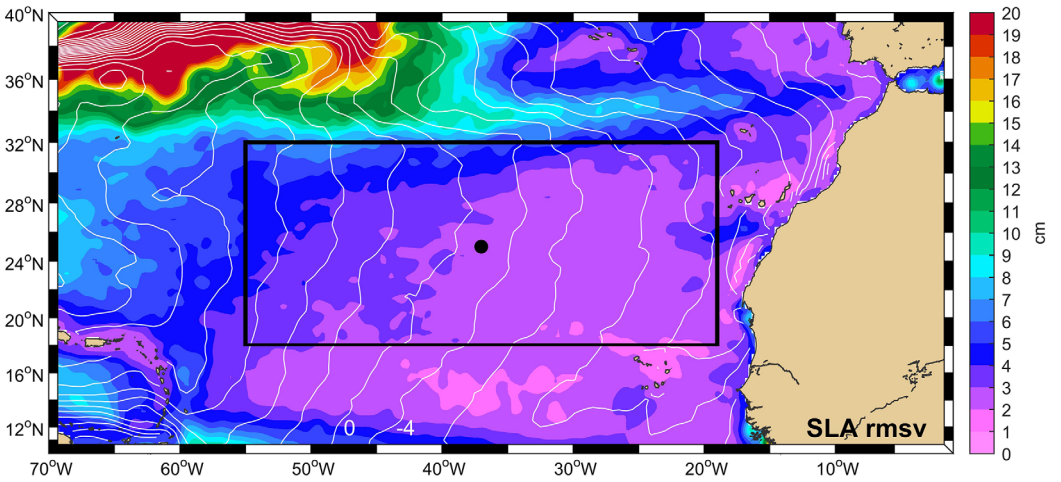

Figure 1. Root mean square variability (color shading) of the 20°-longitude × 10°-latitude spatially high-pass-filtered SLA in the North Atlantic Subtropical gyre based on satellite altimetry data from January 1993 to October 2014. Shown on top are contours (C.I. = 4 cm) of Mean Dynamic Topography (MDT) from *Maximenko et al.* [2009]. The black dot indicates the mean climatological position of the SSS maximum (38°W, 25°N). The black rectangle approximates the interior of the subtropical gyre considered in this study.

negligible effect [*Stammer*, 1998; *Wunsch*, 1999]. This area also coincides with a sea surface salinity (SSS) maximum, located around 25°N and 38°W, with the highest open ocean SSS observed in the World Ocean (Figure 2a). This SSS maximum is mainly caused by an excess of evaporation over precipitation that would be compensated, in a classical explanation, by the Ekman transport [*O'Connor et al.*, 2005; *Schott et al.*, 2004; *Gordon and Giulivi*, 2014]. In this scenario, the surface convergence causes subduction of high salinity water, forming a subsurface "river of salt" [*Qu et al.*, 2013; *Schmitt and Blair*, 2015]. Part of the high salinity water spreads westward and emerges in the Gulf Stream [e.g., *Laurian et al.*, 2009], while the rest is driven to the tropics (Figure 2b) due to the equatorial upwelling, where it gets fresher. Finally, this fresher water is transported back into the subtropics, closing the shallow overturning cell [*Qu et al.*, 2013; *Gordon and Giulivi*, 2014]. However, recent studies have shown that baroclinic eddies may play an important role in setting stratification and distribution of water properties in the subtropical gyres [*Marshall et al.*, 2002; *Gordon and Giulivi*, 2014]. In particular, *Gordon and Giulivi* [2014] argue that the transport of freshwater induced by eddies in the North Atlantic subtropical gyre could significantly compensate the excess of evaporation over precipitation in this region. They concluded that the eddy flux can provide between 50% and 75% of the required freshwater convergence into the SSS maximum, the rest being supplied by the Ekman transport convergence and other ocean processes. Yet, this study was performed relying on model outputs.

The main goal of this paper is to use observational data to characterize the vertical structure and transient transport properties of mesoscale eddies in the interior of the North Atlantic subtropical gyre. As a practical application, we use a box model of the near-surface layer to estimate the role of mesoscale eddies in shaping the distribution of salinity in the SSS maximum. The data sets used and the algorithm developed for computing the eddy composites are described in section 2. Section 3 contains the main results on the vertical structure of the eddies, their transport, and results of the box model. The last section includes the discussion of the results and conclusions.

2. Study Region, Data, and Methods

2.1. Study Region

The mean SSS distribution in the subtropical North Atlantic (Figure 2a) is characterized by the geographically distinct maximum centered near 38°W and 25°N, which we use as an approximate estimate of the gyre center [*Melzer and Subrahmanyam*, 2015]. In order to investigate the vertical structure of mesoscale eddies in the interior of the subtropical gyre and assess their effect on the distribution of salinity in the SSS maximum, a broad study area from 50°−25°W and 16°–32°N (black box in Figure 1) centered on the SSS maximum (black dot in Figure 1) is determined. The northern boundary of the study area, at 32°N, is approximately 200 km away from the mean position of the Azores Current (along ~34°N), associated with a

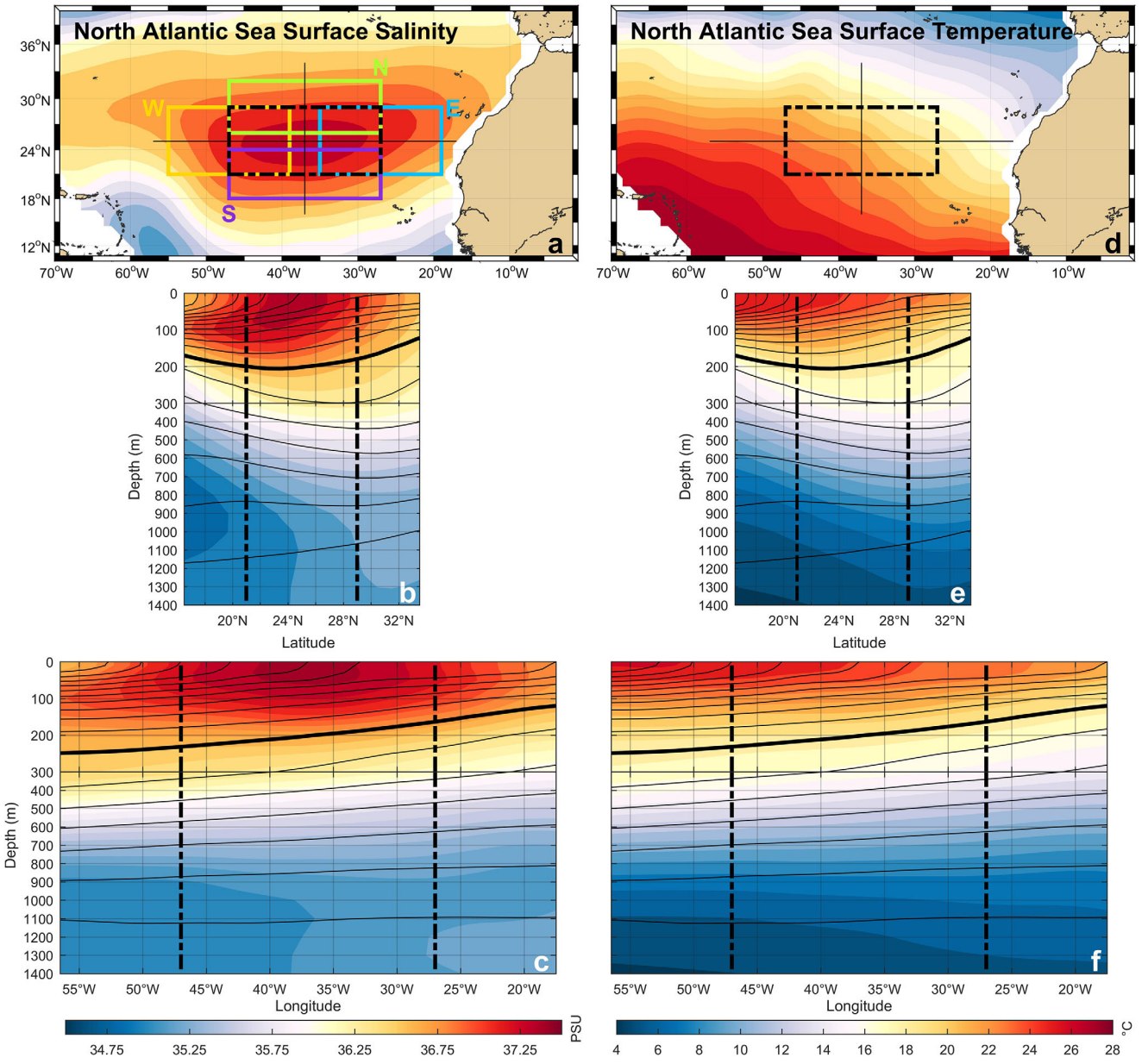

Figure 2. Salinity and potential temperature annual climatology for the North Atlantic Subtropical gyre: (a) SSS (psu). The color-coded rectangles delimit the four different regions where the eddy composites were computed. The dashed black lines delimit the central box where the salinity divergence was computed. (b) Latitude-depth section of the mean salinity (color shading) and potential density (contours; C.I. = 0.2 kg/m^3) along 38° W. The thick solid line (1026.4 kg/m^3) approximates the core of the pycnocline. The dashed black vertical lines indicate the boundaries of the central box. (c) Longitude-depth section of the mean salinity (color shading) and potential density (contours) along 25°N. (d) Mean sea surface temperature (°C). (e) Latitude-depth section of the mean potential temperature (color shading) and potential density (contours) along 38°W. (f) Longitude-depth section of the mean potential temperature (color shading) and potential density (contours) along 25°N. Note that in Figures 2b, 2c, 2e, and 2f, the vertical scale from 0 to 300 m is twice the scale from 300 to 1400 m for better visualization. The locations of the vertical sections plotted in Figures 2b, 2c, 2e, and 2f are denoted in Figure 2a by the thin black lines.

zonal band of enhanced eddy activity between 33°–35°N (Figure 1). In the east, the limiting factor is the presence of the Canary Islands near the African coast, allowing the eastern boundary to be not farther than 19°W. The southern and western boundaries of the study area are then automatically defined in such a way that the area remains centered at the SSS maximum. Figure 1 shows that the area fulfilling the above criteria falls generally within the same dynamical regime; namely, it is entirely in the interior of the subtropical gyre characterized by a broad anticyclonic circulation and relatively weak eddy activity.

Because of the SSS maximum along 25°N, the meridional SSS gradient is southward to the north and northward to the south of 25°N. Likewise, the zonal SSS gradient changes sign from eastward to westward at

around 38°W. To take into account these (and other) changes in the background stratification and examine the variability in the eddy structure across the gyre, the large area defined above is divided into four subareas, structured around the gyre center (Figure 1a). In these subareas, hereafter referred to as box *N* (47°–27°W, 26°–32°N), *S* (47°–27°W, 18°–24°N), *E* (35°–19°W, 21°–29°N), and *W* (55°–39°W, 21°–29°N), the eddy composite analysis is performed following the procedure detailed in section 2.3. Middle sections of the four boxes defined above form the central box (black dashed lines in Figures 2a and 2d). The potential for mesoscale eddies to transport salt in or out of the central box through its lateral boundaries is investigated in section 3.4 using the eddy composites computed in the associated boundary boxes.

2.2. Data

2.2.1. Eddy Data Set

The eddy data set used in this study is that provided by *Chelton et al*. [2011]. It consists of the coordinates of eddy centers, amplitudes, radii, and rotational velocities for the eddies identified and tracked from their surface signature in weekly sea level anomaly (SLA) fields, spanning the period 14 October 1992 to 4 April 2012. We consider this data set to be conservative because it applies some thresholds (eddy life-time longer than 4 weeks, minimum amplitude of 1 cm, etc.; for details see *Chelton et al*. [2011]) that reduce the number of detected eddies but ensure that the remaining structures are real ones. However, these thresholds may also imply removing some real eddies with parameters below the imposed limits. To test the sensitivity of the results to different eddy identification and/or tracking techniques, we tried other algorithms such as *Mason et al*. [2014], *Nencioli et al*. [2010], and *Faghmous et al*. [2015], and found that the results were not very sensitive.

2.2.2. Argo Data and Climatology

Argo is a continuing global array of more than 3000 profiling floats that measure temperature and salinity profiles in the upper 2000 m of the ocean. Most of the floats conduct measurements every 10 days while ascending from the parking depth. Argo profiles collected from 2000 through 2012 in the North Atlantic were used to reconstruct the vertical structure of the eddies. For this purpose, we used the quality controlled Argo profiles included in the *EN4.0.2: quality controlled subsurface ocean temperature and salinity profiles and objective analyses* database [*Good et al*., 2013]. The profile data are provided after having passed a series of quality control procedures, including: implementing Argo quality control flags; removing profiles with locations over land (bathymetric control); checking for density inversions; removing data with impossible depth; and others. A complete description of the quality control procedures applied to the Argo profile data can be found in *Good et al*. [2013].

For the purpose of the present study, some additional quality controls were applied. We discarded the profiles whose positions and times were not flagged as good. From the remaining profiles, only the vertical points flagged as good were retained. Also, the selected profiles had to satisfy the following sampling criteria [*Chaigneau et al*., 2011]. Each profile should at least have 30 vertical measurements and the depth difference between two consecutive measurements in the depth range 0–100 m, 100–300 m, and deeper than 300 m should not be larger than 25, 50, and 100 m, respectively.

For the profiles that passed all the quality controls, we computed the anomalies with respect to the climatological fields obtained from the IPRC Products based on Argo data (http://apdrc.soest.hawaii.edu/projects/argo/). The monthly climatology was determined by averaging monthly mean temperature/salinity fields obtained with variational interpolation of Argo float measurements (http://apdrc.soest.hawaii.edu/projects/Argo/data/Documentation/gridded-var.pdf) at 27 standard levels from 0 to 2000 m depth on a $1° \times 1°$ grid. The temporal coverage used to compute the climatology was 8 years (2005–2012). To compute the anomalies, the original profiles were linearly interpolated into the standard levels and climatological values at the closest point and of the same month were subtracted from the profile data.

2.2.3. Other Data Sets

Daily gridded Sea Level Anomaly (SLA) fields with a global resolution of $1/4° \times 1/4°$ on a Cartesian grid and spatial coverage from 1 January 1993 to 24 October 2014 were obtained from the merged satellite Archiving, Validation, and Interpretation of Satellite Oceanographic data (AVISO) products available at www.aviso.altimetry.fr. The product used here is the delayed time mapped sea level anomaly (SLA) with two satellites merged with the same ground track using a reference period of 20 years (1993–2012). For further details, refer to *AVISO* [2015]. Following *Chelton et al*. [2011], the SLA maps were high-pass filtered with a cutoff wavelength of 20° longitude and 10° latitude to isolate mesoscale variability.

The mixed layer depth (MLD) climatology was downloaded from http://mixedlayer.ucsd.edu. It is available on a 1° grid, computed using Argo profiles and a hybrid method (both the density algorithm and density difference threshold) as described by *Holte et al*. [2010].

The 1° gridded monthly evaporation data set, from 1958 to the present, was obtained from the OAFlux Project (http://oaflux.whoi.edu/evap.html; *Yu* [2007]; *Yu et al*. [2008]).

The 2.5° gridded monthly precipitation data set was retrieved from the Global Precipitation Climatology Project (GPCP) (http://precip.gsfc.nasa.gov/). Precipitation data from various sources are combined into a final merged product that covers a time period from January 1979 to the present [*Huffman et al*., 2009; *Adler et al*., 2003].

2.3. Eddy Composite Computation Algorithm

The mean 3-D structure of mesoscale eddies in a given geographical area was reconstructed using the following procedure:

1. Mesoscale eddies with amplitudes larger or equal to 2 cm and whose centers were located within a given geographical area were selected from the eddy data set. The amplitude threshold of 2 cm was applied in order to discard possible false eddy center detections.
2. For each eddy, we selected Argo profiles whose measurement times occurred within ±3.5 days of the eddy date and were located within a 400 km distance from the eddy center. Their positions were referred relative to the eddy center in a coordinate system $(\Delta x, \Delta y)$, in km, centered at the eddy center.
3. Vertical levels with a relatively small number of observations (compared with the bulk of the water column) were eliminated, resulting in a vertical coverage from 5 to 1400 m (23 standard levels).
4. A dynamic height quality control was performed to eliminate obvious outliers, which could be caused, for example, by erroneous positioning of profiles in the eddy-centered reference frame. For each profile, the dynamic height at the surface was calculated assuming a level of no motion of 1400 m (the maximum available depth). The dynamic heights were sorted as a function of distance to the eddy center and the mean and standard deviation were computed in 10 km bins. In each bin, the profiles with a dynamic height anomaly outside the range of two standard deviations from the bin-average value were excluded from further analysis (this procedure excludes ∼5% of the profiles).
5. Given a set of 2-D points at each vertical level, potential temperature, salinity, and potential density anomaly fields associated with a composite mesoscale eddy were reconstructed by least-square fitting of a orthogonal Fourier series in polar coordinates [*Wang et al*., 2008] as follows:

$$f(r,\varphi)=\sum_{k_{n,m}}\sum_{\alpha=0}^{1}A_{n,m,\alpha}\cdot J_m(k_{n,m}\cdot r)\cdot\sin\left(m\cdot\varphi+\alpha\cdot\frac{\pi}{2}\right) \quad (1)$$

where r and φ are the radial and angular coordinate, respectively, J_m is a Bessel function of the first kind of order m, $A_{n,m,\alpha}$ are the amplitudes of each basis function, and $k_{n,m}$ are the eigenvalues of the radial part. The basis functions in 1 are defined on a finite radius L with zero-value boundary condition, such that $k_{n,m}=x_{n,m}/L$, where $x_{n,m}$ are the positive zeros of J_m. The length scale L was in turn determined from SLA composites obtained by averaging over all SLA snapshots around individual eddies identified in the eddy data set (see Appendix A for details). The basis functions in equation (1) are arranged in descending order of the magnitude of $k_{n,m}$, which also corresponds to the length scale of a particular mode. According to this arrangement, the expansion 1 is truncated to 9 Fourier harmonics (15 different functions taking into account the phase, see supporting information Figure S1), that were sufficient to reproduce the eddy structure. Introducing higher-order Fourier harmonics resulted in small-scale features that were related to errors in the data rather than real physical processes. After computing the amplitudes $A_{n,m,\alpha}$, by linear fitting the available observations at every vertical level, the anomaly fields of the composite eddy were reconstructed on a regular 5 × 5 km grid using the functional form 1.

1. The salinity and potential temperature anomalies associated with the eddy composite were scaled to match the resulting eddy amplitude in dynamic height (computed from the associated potential density anomalies) to the mean eddy amplitude in SLA maps (last row in Table 1; see an example in Figure 10d). Here we assume that both the potential temperature and salinity anomalies and the magnitude of SLA in the average eddy are linearly correlated [*Castelao*, 2014; *Souza et al*., 2011; *Frenger et al*., 2015]. The

Table 1. Main Eddy Properties Computed From the Eddy Data Set [*Chelton et al.*, 2011] in the Four Subregions in the Interior of the North Atlantic Subtropical Gyre (Figure 2a)[a]

	West		North		South		East	
	Cyc	Ant	Cyc	Ant	Cyc	Ant	Cyc	Ant
Amplitude (cm)	3.7 (59%)	3.3 (58%)	4.6 (64%)	2.9 (61%)	3.2 (59%)	2.8 (58%)	3.0 (61%)	3.1 (63%)
Radius (km)	97.2 (55%)	97.3 (56%)	88.7 (57%)	92.0 (55%)	102.5 (58%)	102.0 (57%)	94.2 (58%)	89.4 (59%)
Rot. Speed (cm/s)	10.3 (56%)	9.6 (56%)	10.8 (61%)	8.0 (56%)	9.6 (58%)	9.0 (54%)	8.4 (56%)	9.1 (60%)
Prop. Distance (km)	586.9 (70%)	421.0 (68%)	554.1 (70%)	290.5 (71%)	485.0 (69%)	386.5 (68%)	353.7 (70%)	303.0 (70%)
Life (days)	162.4 (69%)	126.4 (68%)	188.9 (68%)	111.6 (72%)	117.5 (68%)	106.5 (69%)	107.8 (69%)	97.7 (66%)
Trans. Speed (cm/s)	3.8 (52%)	3.6 (51%)	3.0 (52%)	2.8 (50%)	4.5 (52%)	4.1 (53%)	3.5 (55%)	3.5 (52%)
# Eddies/day	6.1 (61%)	5.9 (42%)	6.5 (49%)	4.3 (57%)	5.3 (57%)	4.9 (40%)	5.9 (41%)	5.5 (51%)
SLA eddy Amp. (cm)	6.7	6.2	7.7	6.2	4.7	4.7	5.1	5.4

[a]Accumulated probability below the mean value is shown in parentheses to note the cases in which the probability distribution is not symmetric. Last row shows the amplitudes of the SLA eddy composites. These SLA composites were obtained by averaging over all snapshots cut around individual eddies identified in the eddy data set.

scaling is selected to correspond to the SLA composites rather than to the mean eddy amplitudes from the eddy data set because it is known that the latter are underestimated [*Chelton et al.*, 2011]. The potential density anomaly field was recomputed, taking into account the scaled salinity and potential temperature anomalies and the mean background salinity and potential temperature profiles.

2. At each vertical level and grid point, the dynamic height was computed with a reference depth of 1400 m. The associated velocity fields were calculated using the thermal wind relation with the same reference depth. Finally, the origin of the coordinate system was adjusted to coincide with the maximum (minimum) in sea surface dynamic height for the anticyclonic (cyclonic) composite, defining the eddy center.

3. Results

3.1. Mean State

To examine the large-scale water mass distribution in the study region, Figure 2 shows cross sections of the mean salinity, potential temperature, and potential density across the subtropical gyre. In the subtropical regime, the highest salinity is observed near the surface as a result of strong evaporation. A subsurface salinity maximum at around 100 m depth is clearly visible in the equatorward part of the subtropical gyre, caused by the subduction of high salinity water from the center of the gyre [*Talley*, 2002; *Schmitt and Blair*, 2015]. The main thermocline extends from about 100 to 600 m depth and is a bit deeper in the northern part of the domain. A prominent feature of the thermocline, particularly in the northern part of the domain, is the presence of a nearly isothermal layer in the depth range 100–300 m, which signifies the North Atlantic Subtropical Mode Water [*Hanawa and Talley*, 2001]. The isopycnals deepen from south to north in the southern part of the domain and from north to south in the northern part (Figure 2b), reflecting the bowl shape of the pycnocline in the subtropical gyre. In the zonal direction (Figures 2c and 2f), the isopycnals are tilted from east to west, indicating southward geostrophic flow, consistent with the Sverdrup balance [*Sverdrup*, 1947]. These horizontal gradients of potential density are indicative of available potential energy of the mean flow, which is a likely source of eddy variability in the region [*Spall*, 2000; *Gill et al.*, 1974].

3.2. Eddy Statistics

Prior to analyzing the vertical structure of mesoscale eddies in the subtropical North Atlantic, it is instructive to have a closer look at their mean properties at the sea surface as identified in SLA fields [*Chelton et al.*, 2011]. The mean eddy properties in each defined area (W, N, S, and E in Figure 2a) are summarized in Table 1. Numbers in parentheses indicate the accumulated probability below the mean value and characterize the asymmetry and effect of "tails" in the statistical distributions, as reported by *Chelton et al.* [2011]. The mean eddy amplitudes in the eddy data set range between 2.8 and 4.6 cm, reflecting the low eddy kinetic energy character of the study area. On average, cyclonic eddies possess slightly larger amplitudes than anticyclonic eddies, except for the eastern part of the domain (box E), where the parameters of cyclonic and anticyclonic eddies are nearly the same. The most significant differences are found in box N where the cyclones are about 30% stronger than anticyclones. The average number of cyclones and anticyclones per day inside a given region, computed as a ratio between the total number of eddies inside that region and

the total number of days in the observation period (1992–2012), ranges between 4.3 and 6.5, with a slightly larger number of cyclones in all regions (Table 1).

Eddies in the study domain have typical radii of around 95 km, varying weakly with latitude from about 102 km in the southern part of the domain (box S) to 90 km in the northern part (box N) with no significant differences with respect to eddy polarity. We also observe that the average eddy lifespan is about 3 months and average propagation distance is less than 300 km (∼3 degrees of longitude). These distances are much smaller than the dimensions of our boxes (Figure 2a), indicating that in each subregion eddies are generated mainly locally, presumably by means of baroclinic instability of the mean flow [*Gill et al*., 1974].

The last row in Table 1 lists the mean eddy amplitudes determined from their SLA composites as extremum values at the eddy centers (Appendix A). The amplitudes defined in this manner are about 60% larger than the average eddy amplitudes in the eddy data set. The discrepancy between the two estimates is mainly due to the choice of a reference level. In the eddy composite analysis the average amplitudes are determined relative to a reference of zero SLA, while in the eddy data set the eddy amplitudes are determined relative to some ambient SLA around the eddy periphery [*Chelton et al*., 2011]. The latter choice may result in some underestimation of the true eddy amplitudes [*Chelton et al*., 2011].

3.3. Composite Eddies and Associated Fluxes

3.3.1. Vertical and Horizontal Eddy Composite Structures

The zonal sections across the composite eddies in the four subregions are shown in Figure 3. Except for the near-surface layer, the structure of the anomalies along the eddy vertical axes corresponds to the mean T-S profiles (Figure 4) perturbed by uplifted (depressed) isopycnals typically associated with the cyclonic (anticyclonic) eddy.

The thermal structure of the composite cyclones (anticyclones) in the four areas is generally characterized by a cold (warm) anomaly of about 1°C peaking within the thermocline layer at around 150 m and extending down to much greater depths. A secondary peak can be found from 400 to 800 m below the surface, which is consistent with the background stratification showing enhanced vertical gradients of the mean potential temperature in this layer (Figure 2). Note also that cyclones and anticyclones have very similar temperature anomaly patterns, consistent with the notion that the anomalies at depth are closely related to the eddy-induced displacements of the average isopycnal surfaces.

The cyclonic and anticyclonic eddies are also characterized by large salinity anomalies, which, except for the near-surface layer, correspond closely to the temperature anomaly patterns and appear to be a consequence of the eddy-induced vertical displacements of the average isopycnal surfaces. They also demonstrate that, despite being relatively weak in SLA (Figure 1), the eddy signal penetrates to at least 1200 m depth, which is clearly seen in the eddy-induced salinity anomalies at the depth of the Mediterranean Water (MW). In the cyclones for all four areas, for example, salinity anomaly is positive below 800-1000 m depth (Figured 3c, 3g, 3k and 3o). This level coincides with the depth of a salinity minimum in the mean T-S diagram (Figure 4) followed by a salinity maximum at around 1200 m depth associated with the MW. Due to the doming of the isopycnal surfaces induced by the average cyclonic eddy, the high salinity waters associated with the MW are lifted to a shallower layer, creating positive salinity anomaly in the depth range 800–1000 m (Figures 3c, 3g, 3j and 3o). The same mechanism, acting in the opposite direction, can be used to explain deep salinity anomalies in the average anticyclonic eddy. Due to the depression of the isopycnal surfaces in the anticyclonic eddy, the low salinity waters associated with the intermediate layer (800–1000 m) are pushed deeper, resulting in negative salinity anomaly in the depth range of the MW.

In general, the cyclonic (anticyclonic) eddies are characterized by cold (warm) and fresh (salty) anomalies whose effects on the density field are partly compensated. However, because the effect of temperature on density is much larger than that of salinity, the resulting potential density anomalies are large (thin solid and dashed lines in Figure 3) and correspond closely to the potential temperature anomalies. Yet, the patterns do not coincide, indicating that salinity also plays a role, particularly in the near-surface layer. Consistent with the distributions of the potential density anomaly, the eddy velocities are surface-intensified and vertically coherent through the water column, decaying with depth. The maximum rotational speeds are observed at a distance of about 90–100 km from the corresponding eddy centers, consistent with estimates from the eddy data set (Table 1). The cyclonic and anticyclonic eddies have similar velocity structures with

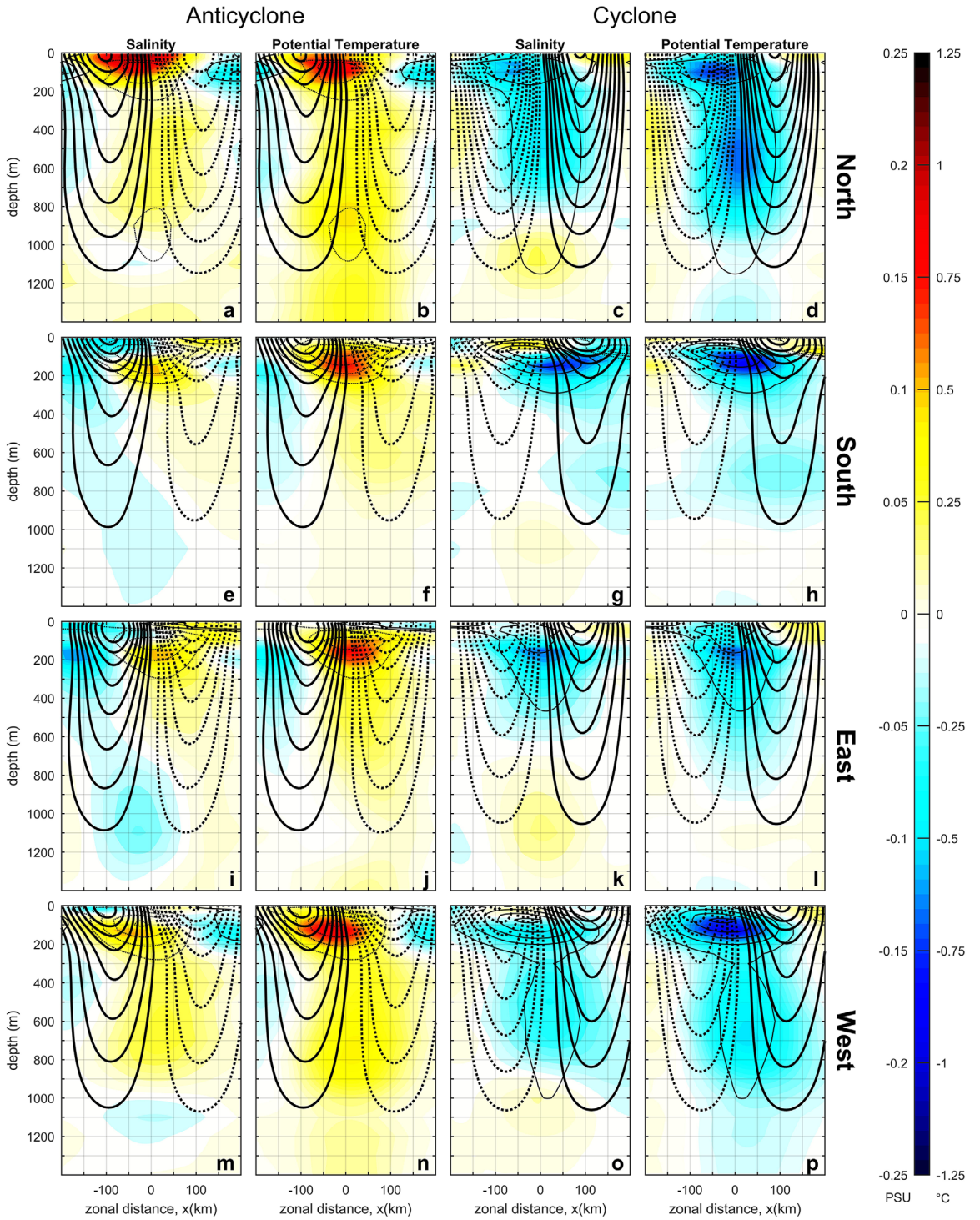

Figure 3. Zonal sections across the composite eddies in the four subregions delimited in Figure 2a. Each row corresponds to one region. The first two (third and fourth) columns show salinity (psu) and potential temperature (°C) anomaly for the anticyclonic (cyclonic) eddy composite. Thick solid (dashed) lines show positive (negative) meridional velocity (C.I. = 1 cm/s). Thin solid (dashed) lines show positive (negative) potential density anomaly (C.I. = 0.04 kg/m^3). Note the vertical tilting of the velocity field in the upper layers, observed in the inclination of the consecutive minimums of the velocity isolines, for example in panel m.

the exception of the composites in the northern subregion, where the cyclones are slightly stronger than the anticyclones, in agreement with the eddy statistics computed from the eddy data set (Table 1). Moreover, a remarkable characteristic of the eddy composites in Figure 3 is the vertical phase tilts in the upper

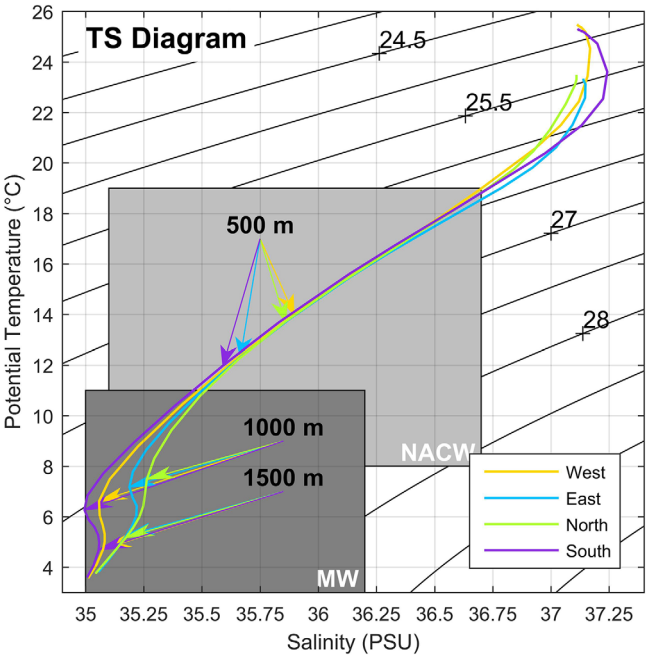

Figure 4. Potential temperature versus salinity (T-S) diagrams based on the climatological profile data in the four subregions (Figure 2a). The depths of 500, 1000, and 1500 m are marked by arrows. Contours show potential density (C.I. = 0.5 kg/m^3). Properties of the North Atlantic Central Water (NACW) and the Mediterranean Water (MW) are marked by the grey boxes (from *Emery and Meincke* [1986]).

~200 m, particularly evident in the eddy velocity structure (e.g., Figure 3m), that indicates that horizontal variations in the eddy structure are dynamically important.

The horizontal structure of the eddy-induced salinity anomaly at different depths for the cyclonic composite eddy in the northern subregion is shown in Figure 5. Although the eddy structures vary from one area to the other, only this case will be discussed in detail here because it is the most illustrative and similar conclusions can be applied to the rest of the areas. At the sea surface, the eddy-induced salinity anomaly can be characterized by a dipole structure (see, also, Figure 6a) where the leading (western) pole is somewhat larger in magnitude and closer to the eddy center than the trailing (eastern) pole. Such a dipole structure is consistent with the interpretation of the anomalies as being caused by horizontal advection of the background temperature/salinity gradient by the eddy rotational velocities [*Chelton et al.*, 2011; *Gaube et al.*, 2015]. The effect of advection is clearly observed in the surface salinity anomaly field of the composite cyclone (Figure 5) showing a well pronounced dipole structure with a positive lobe located in the north-east quadrant and a negative lobe located in the south-east quadrant. The mean SSS distribution in the study area (Figure 2a), shows that such a dipole pattern appears when the cyclonic eddy advects saltier waters from south to north on its eastern side and fresher waters from north to south on its western side. With increasing depth, however, the dipole loses its strength and the negative anomaly converges toward the center of the eddy (Figure 5b). This occurs because the rotational velocities of the eddy weaken with depth and because the mean isohalines become flatter (see the mean salinity distribution near the northernmost vertical line in Figure 2b), so that the advection effects disappear. With the disappearance of the dipole, the dominant relevant process is elevation of the isopycnals that leads to the emergence of the monopole structure centered on the eddy core.

The geometric decomposition of the eddy anomaly field into a monopole and dipole structure is visualized in Figure 6. Figures 6a and 6e show the salinity anomaly for the composite cyclone at 5 and 600 m depth, respectively. The monopole and dipole structures at both depths are shown in Figures 6b and 6f, and 6d and 6g, respectively, and were computed by setting to zero the amplitudes of all the basis functions except for those corresponding to either a monopole or dipole (see supporting information Figure S1). The reconstructions by a linear combination of the monopole and dipole are shown in Figures 6d and 6h. In the surface layer (Figures 6a–6d), the dipole dominates the horizontal structure of the eddy composite. The negative anomaly monopole related, presumably, to the elevation of the isopycnals in the eddy core, contributes to the combined structure by making the negative lobe stronger and slightly displacing it toward the eddy center. At 600 m depth (Figures 6e–6h), the monopole dominates the horizontal structure, while the dipole has almost disappeared. The reconstructed fields (Figures 6d and 6h) closely follow the original fields, indicating that the main features of the eddy composites can well be characterized by taking into account the two dominant physical processes: vertical displacements of the isopycnal surfaces in the eddy core (monopole) and the horizontal advection of the background gradient by rotational eddy velocities (dipole).

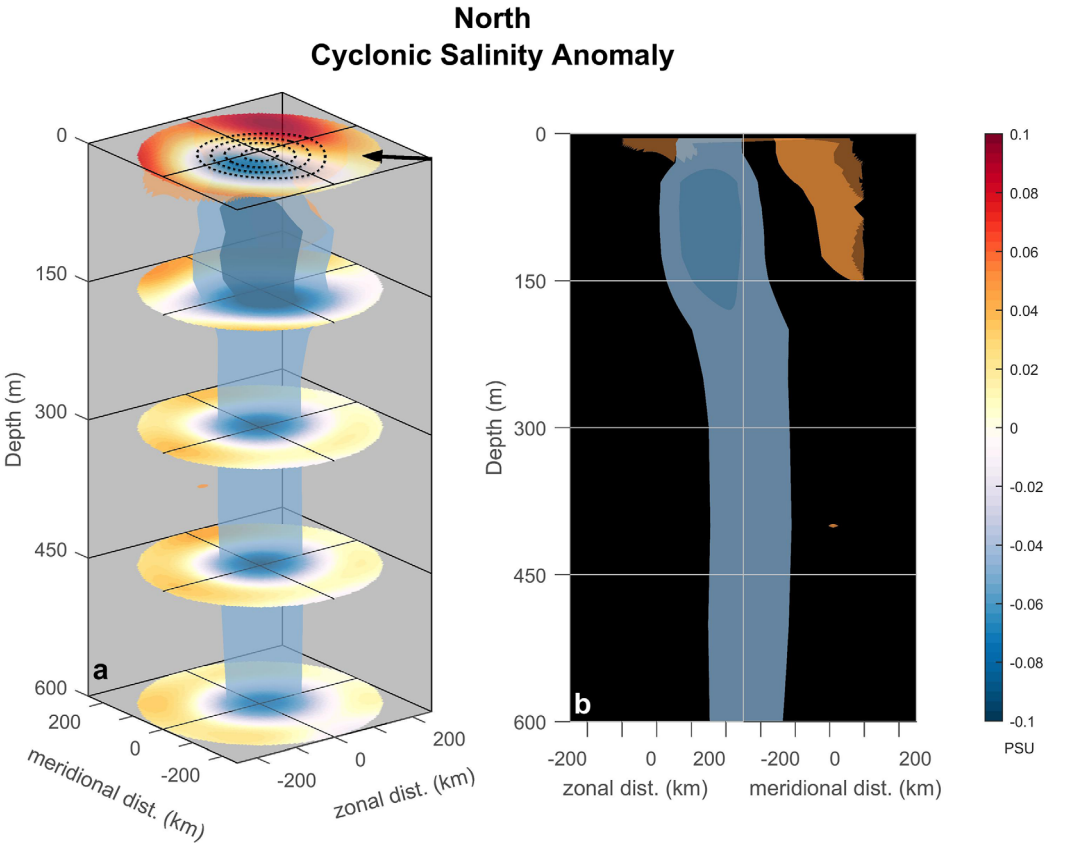

Figure 5. Three-dimensional structure of the eddy-induced salinity anomaly (psu) for the cyclonic composite eddy in box N (Figure 2a). The isosurfaces are −0.1 and ±0.05 psu. The horizontal slices in Figure 5a are shown at five different depths: 0, 150, 300, 450, and 600 m. Contours at the surface (z = 0 m) show dynamic height anomaly relative to 1400 m depth (C.I. = 2 cm; zero contour is omitted). Figure 5b shows the same field but from the point of view of the arrow in Figure 5a. It allows observing the transition from a dipole-dominated anomaly structure in the near-surface layer (<150 m) to a monopole-dominated structure at greater depth. Note that left part of the "horizontal axes" refers to the zonal distance and the right part to the meridional distance.

3.3.2. Mean Salt and Heat Fluxes

The dipole structure in the temperature/salinity anomaly composites is related to lateral phase shifts between pressure and temperature/salinity perturbations in the eddy, providing a mechanism for the eddy heat/salt flux [*Hausmann and Czaja*, 2012; *Frenger et al.*, 2015]. Note also the vertical tilts in the composite eddies (Figure 3), which correspond to a necessary condition for the geostrophic eddies to have net heat/salt transport [*Bennett and White*, 1986; *Roemmich and Gilson*, 2001]. Following *Hausmann and Czaja* [2012], the heat and salt transports across the average eddy are estimated as:

$$
\begin{aligned}
F_{heat}^{zonal}(z) &= C_p \cdot \rho_0(z) \cdot \int_{-L_f}^{L_f} u'(x=0,y,z) \cdot \theta'(x=0,y,z)\, dy \\
F_{heat}^{meridional}(z) &= C_p \cdot \rho_0(z) \cdot \int_{-L_f}^{L_f} v'(x,y=0,z) \cdot \theta'(x,y=0,z)\, dx \\
F_{salt}^{zonal}(z) &= \int_{-L_f}^{L_f} u'(x=0,y,z) \cdot S'(x=0,y,z)\, dy \\
F_{salt}^{meridional}(z) &= \int_{-L_f}^{L_f} v'(x,y=0,z) \cdot S'(x,y=0,z)\, dx
\end{aligned}
\tag{2}
$$

where u' and v' are the eddy composite zonal and meridional velocity, respectively, θ' is the eddy potential temperature anomaly, S' is the eddy salinity anomaly, C_p is the specific heat capacity (4000 J·kg^{-1}·K^{-1}), and $\rho_0(z)$ the mean climatological potential density profile over the area where the

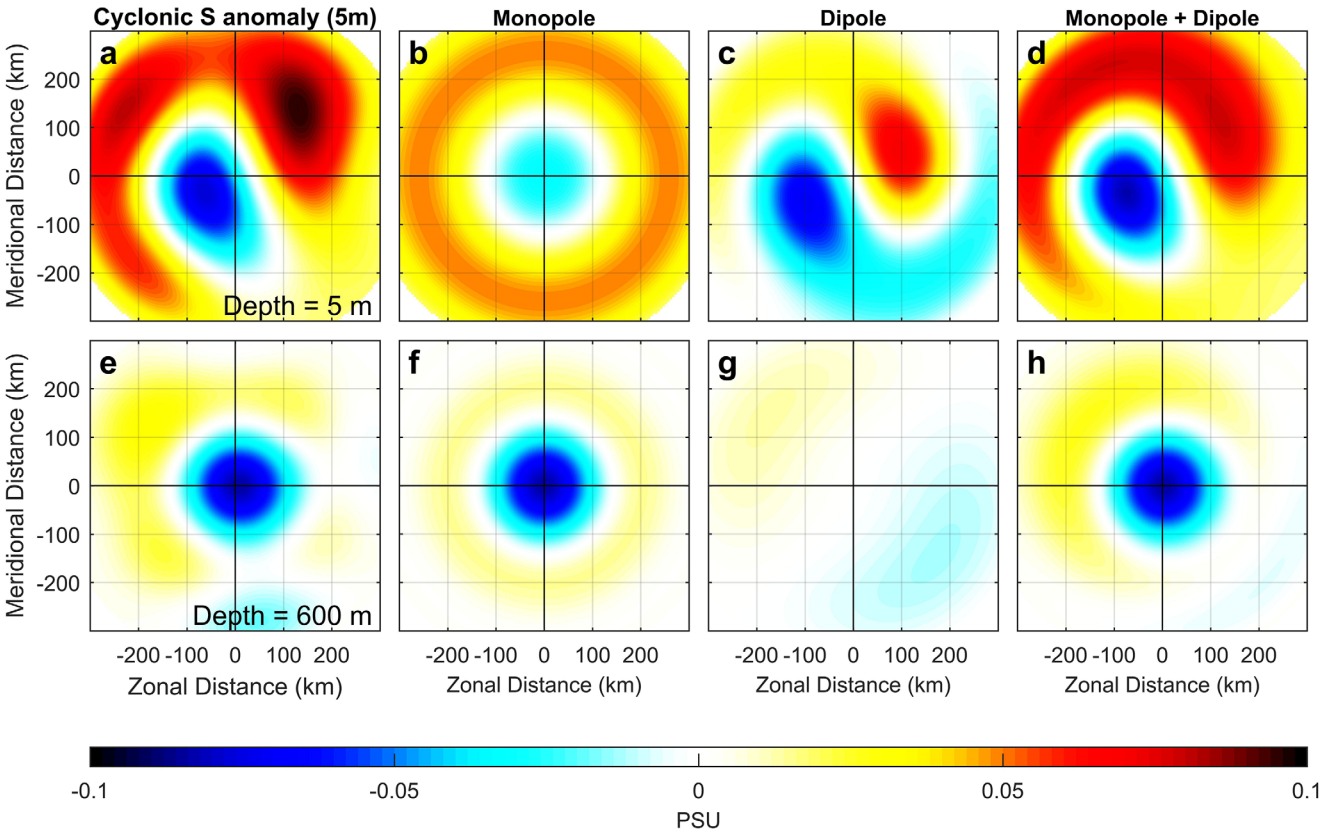

Figure 6. Approximation of salinity anomaly composite of the cyclonic eddy in the northern subregion (box N; Figure 2a) at (a) 5 m depth and (e) 600 m depth as a sum of a monopole (b and f) and a dipole (c and g). The approximated structures are shown in Figures 6d and 6h, respectively.

eddy composite was computed. The choice of a value for the eddy length scale L_f is made to ensure that the mass transport across the eddy is zero; thus it is set to the distance where the surface velocity field decays to zero ($\sim$200 km).

The resulting estimates of the heat and salt transports induced by the composite eddies, cyclonic, and anticyclonic combined, are shown in Figures 7a–7h (thick lines). A common feature in all four areas is that the eddy-induced transports are the largest above the thermocline ($<$200 m) and then quickly decay with depth. This decay of the eddy transport with depth can be attributed to the weaker potential temperature and salinity gradients on the deeper isopycnal surfaces (Figure 2), the decay in the magnitude of the eddy-induced salinity/temperature anomalies, the weakening of the eddy velocity field (Figure 3), and the structural changes in the salinity/temperature anomaly fields associated with a transition from a dipole to a monopole-dominated structure. The fluxes have also been estimated from the eddy composites reconstructed with a linear combination of only a monopole and dipole structures (thin lines in Figure 7). The results were very similar to those computed with the full Fourier series (thick lines), and therefore, the basic eddy structure and its associated fluxes are mainly determined by a combination of the vertical displacements of isopycnal surfaces in the eddy core (monopole) and the horizontal advection of the background field due to the eddy rotational velocities (dipole).

The magnitude and direction of the eddy flux appear to be closely related to the magnitude and direction of the background gradient of the corresponding property, in agreement with a classical downgradient mixing hypothesis. As example, Figure 7i shows the eddy heat fluxes in the top 50 m layer (arrows) on top of the map of the mean mixed layer temperature. Evidently, the heat fluxes are directed down the mean SST gradient and the role of eddies in the surface layer is to transport heat poleward. The same arguments are valid for the eddy salt fluxes (Figure 7j). The fluxes are directed down the mean SSS gradient, in all four boxes pointing away from the SSS maximum. The role of eddies, therefore, is to flux salt out of the subtropical

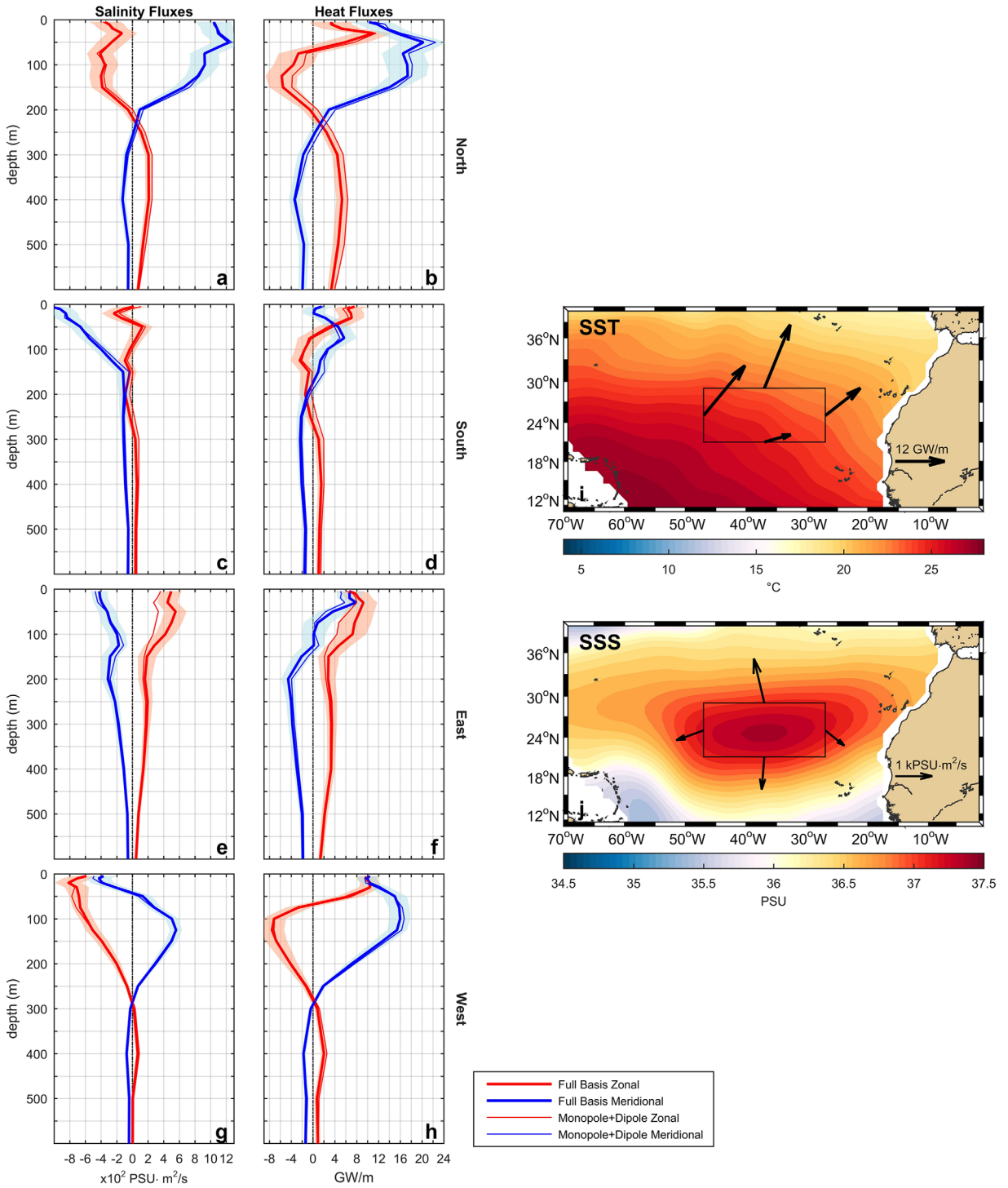

Figure 7. Salt (a, c, e and g) and heat (b, d, f and h) fluxes associated with the composite eddies (cyclonic and anticyclonic combined) in the four subregions delimited in Figure 2a. Thick and thin lines correspond to the eddy composites reconstructed using full series (equation (1)) and only a superimposition of the monopole and dipole, respectively (see text for detail). Each row corresponds to one region. Shaded areas denote the uncertainty estimates (see Appendix B for details). (i) Eddy heat fluxes in the upper 50 m layer (arrows) shown on top of the map of the mean mixed layer temperature. (j) Eddy salt fluxes in the upper 50 m layer (arrows) shown on top of the map of the mean mixed layer salinity.

gyre in order to compensate for the increase of salinity due to the excess of evaporation over precipitation [*Gordon and Giulivi*, 2014; *Tréguier et al.*, 2014]. To quantify this effect, we use a simple box model of the near-surface layer in the subtropical gyre, which is a subject of the next section.

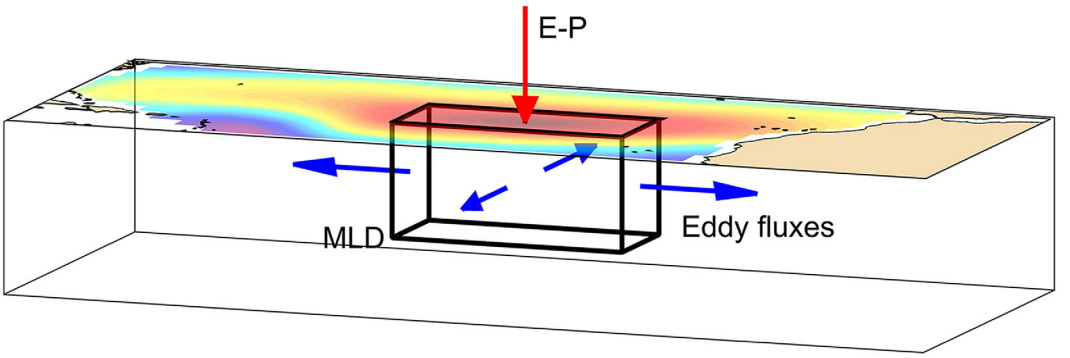

Figure 8. Schematic of a box model used to estimate the role of mesoscale eddies in shaping a quasi-steady distribution of salinity in the North Atlantic subtropical salinity maximum.

3.4. Application to the Subtropical Salinity Maximum: A Box Model

To estimate the eddy contribution to the quasi-steady state distribution of salinity in the North Atlantic SSS maximum, we use a box model of the near-surface layer. A schematic illustration is given in Figure 8. The box is centered on the SSS maximum. The lateral boundaries of the box (47–27°W, 21–29°N) coincide with the middle sections of the boxes where the eddy composites were computed (Figure 2a). In the vertical, the box is set to correspond to the mixed layer depth (MLD), and can vary seasonally from ~25 m in summer to ~100 m in winter months. Following the approach by *Gordon and Giulivi* [2014], we consider the salt (or, equivalently, freshwater) budget in the box and estimate the relative contribution of the eddy transport as a fraction of the surface flux (E-P). This allows us to avoid closing the salt budget for which our box model is too simplistic. In particular, we are not taking into account vertical processes at the base of the mixed layer, and we assume that the eddy contribution to balancing the E-P flux is confined to the mixed layer. It is worth mentioning, however, that the horizontal eddy fluxes in the layers below the mixed layer (down to 150 m or deeper (Figure 7), as pointed out by one of the anonymous reviewers) may contribute to the mixed layer salt budget too, by working to reduce the maximum salinity gradients in the subsurface layers, which would also affect the surface layer salinity through vertical entrainment and mixing.

The "virtual salt flux" due to E-P [*Gill*, 1982; *Farrar et al.*, 2015], F_{E-P}, was computed as:

$$F_{E-P} = \frac{1}{H}\int_{A_s} (E(x,y) - P(x,y)) \left[\int_{-H}^{0} \overline{S(x,y,z)}\, dz\right] dA_s \tag{3}$$

where E is evaporation, P is precipitation, H is MLD, A_s is the surface area of the box, and $\bar{S}$ is the climatological salinity inside the box. The eddy salt flux divergence in the box, F_{eddy}, is estimated as the sum of the fluxes through the four lateral boundaries of the box:

$$F_{eddy} = \sum_{i=1}^{4} \int_{A_i} \overline{S'\mathbf{u}_\mathbf{h}'} \cdot d\mathbf{A}_{h_i} \tag{4}$$

where S' is the eddy salinity field, $\mathbf{u}_\mathbf{h}'$ is the horizontal eddy velocity, A_i is the area of each one of the lateral boundaries of the box, and the overbar denotes the time mean.

The eddy composites reconstructed in the four areas (section 3.3) were used to estimate the eddy fluxes through the box's lateral boundaries. Two approaches were used to provide a lower and upper bound estimates. The first approach utilizes the 3-D eddy composites and combines them with the statistics of eddy locations, polarities, amplitudes, etc., derived from the eddy data set of *Chelton et al.* [2011]. The eddy salt fluxes in equation (4) were reconstructed as follows:

1. Each individual eddy identified in the eddy data set in a given area (N, S, E, or W) and at a given time (date) was associated with its 3-D composite, according to the eddy polarity and amplitude. The scale factor for each eddy was defined as $\eta = (A_{eddy}/A_{ed.comp.})^2$, where A_{eddy} was the eddy amplitude in the eddy data set and $A_{ed.comp.}$ was the amplitude of the composite eddy defined as the dynamic height at the eddy center.

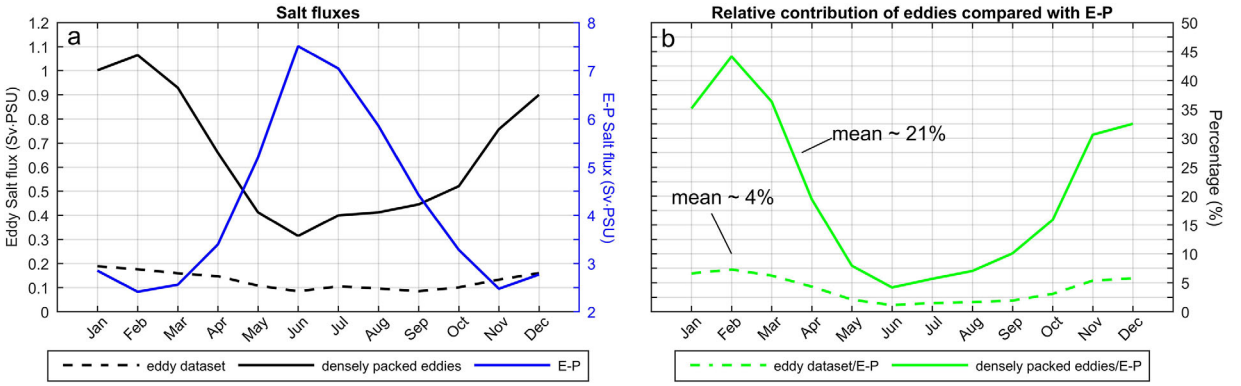

Figure 9. (a) Seasonal variability of the salt flux divergence in the subtropical box (Figure 8). Black lines (left axis) show the eddy salt flux divergence computed using real eddy trajectories from the eddy database by *Chelton et al*. [2011] (dashed) and the densely packed eddies assumption (solid). The two provide lower and upper bound estimates, respectively (see text for detail). The blue line (right axis) shows the *virtual salt flux* due to E-P. (b) Percentage of the E-P salt flux compensated by the eddy salt flux divergence. The dashed (solid) line corresponds to the lower (upper) bound estimate of the eddy salt flux. The mean over the year values are 11% and 21%, respectively.

2. The product of the velocity anomaly and salinity anomaly, $S'\mathbf{u}_\mathbf{h}'$, was determined for each individual eddy and positioned according to the eddy location (at a given time) in the eddy data set.
3. All the "one-eddy" fields from the previous step were added together to obtain a 3-D eddy salinity flux field for each available day. All the days from the same month were averaged to obtain monthly climatology. The flux fields through the lateral boundaries of the box (Figure 8) were then obtained from the associated 3-D distributions. To increase the statistical accuracy of the estimates, the flux fields were averaged across each section over a ∼200 km thick lateral layer (approximately the diameter of the average eddy).
4. Finally, the integrated fluxes across the boundaries of the box in equation (4) were estimated for each climatological month given the corresponding MLD.

The above approach is thought to provide a lower bound estimate of the eddy fluxes because the weekly data set retains only long-lived eddies (lifetimes >4 weeks) with amplitudes larger than 1 cm, it allows multiple SLA extremes inside one eddy, and may also underestimate the eddy amplitudes [*Chelton et al*., 2011].

In the second approach, the ocean is assumed to be populated with densely packed eddies. Any given zonal or meridional section can thus be viewed as a chain of eddies with alternating polarity. All eddies in this sequence are assumed to be geometrically and dynamically similar. The average effect of eddies can then be represented by a single "typical" eddy [*Thompson and Young*, 2006] and the eddy flux through the section is given simply by the associated *per eddy* flux as a function of depth (Figure 7) multiplied by the number of eddies that can fit into the section length. For this task, the eddy width was set at 400 km (twice the radial distance at which the eddy rotational speed decays to zero (Figure 3)) and the fluxes through the box in equation (4) were estimated for each climatological month, taking into account the seasonal cycle in MLD. This approach is thought to give an upper bound estimate as it may significantly overestimate the number of eddies present at a given time in the region.

It is worth mentioning that estimates made with the first approach take into account monthly climatological changes in the eddy amplitudes, number of eddies, and MLD, while the second approach only incorporates seasonal variations in MLD.

The salt flux due to E-P (equation (3)) and the one due to eddies (equation (4)), computed with both approaches detailed above, are shown in Figure 9a. As expected, the eddy salt flux divergence estimated from the densely packed eddies assumption (solid black line) is always larger than that estimated from the eddy trajectories in the eddy data set (dashed black line). Despite the difference in the magnitude, both estimates present a minimum in summer and a maximum in winter, which reflect the seasonal cycle in the MLD (minimum around 25 m in June and maximum around 100 m in February). If the effect of the MLD seasonality is removed, e.g., by fixing the MLD to a constant value of 50 m, the eddy salt flux divergence computed from the eddy trajectories reverses its behavior (not shown), with a maximum in summer (0.16 *Sv* · *PSU*) and a minimum in winter (0.10 *Sv* · *PSU*). These changes are a consequence of the seasonality in the number and intensity of eddies, both having a maximum in summer and a minimum in winter.

The MLD seasonality, with a reversed effect, is also reflected in the seasonal behavior of the surface flux due to E-P (blue solid curve in Figure 9a). The maximum (minimum) F_{E-P} (equation (3)) is observed in summer (winter) when the ML is the shallowest (deepest) and thus a smaller (larger) volume of water is subject to salinification due to excessive evaporation.

The relative contribution of the eddies to compensate for excessive evaporation in the North Atlantic subtropical salinity maximum is shown in Figure 9b. The figure shows that summer is the season when the eddy contribution is the smallest, with the lower and upper bound estimates being around 1% and 4%, respectively. This minimum can largely be explained by the minimum in the MLD in the summer months. The maximum contribution of the eddies coincides with the moment of the deepest MLD, in February, with the values between 8% (lower bound estimate) and 45% (upper bound estimate). The yearly averages are 4% and 22%, respectively. These would increase to 6% and 29%, respectively, if the effect of the varying volume of the subtropical box was taken out by using the annual mean MLD of 50 m.

4. Summary and Discussion

Salinity and temperature profile data from the Argo float array have been combined with the eddy database by *Chelton et al*. [2011] to reconstruct 3-D eddy composites in the interior of the North Atlantic subtropical gyre on the four flanks of the SSS maximum. The composites were used to study eddy vertical and horizontal structures, their transient salt and heat fluxes, and to estimate the relative contribution of the eddy transport to compensate for the local excess of evaporation over precipitation, characteristic of the study area.

Signals in velocity, potential temperature, and salinity anomaly of the eddy composites in the four areas studied here extended below 1000 m depth, suggesting that the influence of eddies may be important, despite their relatively low signal in SLA maps ($\sim$5 cm; Figure 1). In particular, the signature of the Mediterranean Water was clearly observed in the eddy-induced salinity anomaly at around 1000 m depth.

The horizontal structure of the average eddy can be explained by a linear combination of a monopole and dipole structure. The monopole would be related to the depression (elevation) of the isopycnal surfaces typically associated with the anticyclonic (cyclonic) eddy; the dipole would reflect the effect of horizontal advection of the background temperature/salinity gradient by the rotational velocity of the eddy [*Chelton et al*., 2011; *Gaube et al*., 2015]. In the upper $\sim$200 m layer, above the thermocline, the effect of horizontal advection dominates, while below the thermocline (depth $>$ 300 m), vertical displacements of mean isopycnal surfaces are mostly responsible for the anomaly patterns.

The dipole structure in the eddy composites is related to the lateral phase alignment between the temperature/salinity and velocity anomaly fields, providing a mechanism for the eddy heat/salt flux [*Hausmann and Czaja*, 2012; *Souza et al*., 2011]. Consistent with a rapid decay of the eddy-induced temperature/salinity anomalies and velocity perturbations with depth, the eddy fluxes in the study area are surface-intensified and confined mainly to the upper 200 m layer (Figure 7). The magnitude and direction of the eddy heat and salt fluxes appear to be closely related to the horizontal gradients of the corresponding property, consistent with a downgradient mixing hypothesis. Eddy heat fluxes are mainly poleward, while eddy salt fluxes transport salt out of the SSS maximum area, partly compensating for the salinity increase due to the excessive evaporation over the area [*Gordon and Giulivi*, 2014]. It is important to emphasize that these eddy fluxes are due to internal eddy structure, resulting in nonzero correlations between temperature/salinity and velocity perturbations over the eddy "wavelength" [*Roemmich and Gilson*, 2001; *Qiu and Chen*, 2005; *Souza et al*., 2011], and not a consequence of "trapped water" carried by eddies along their trajectories [*Flierl*, 1981; *Early et al*., 2011]. Because most eddies in the study area propagate only short distances ($\sim$350 km; Table 1), comparable to their own size, and the background gradients of water properties are smooth (no narrow fronts which eddies would cross), the effect of nonlocal transport due to trapped water is expected to be insignificant and may not need additional consideration [*Frenger et al*., 2015]. There is a possibility that few eddies formed in the coastal region with quite different water properties and dynamics (e.g., "mode" anticyclones identified by *Schütte et al*. [2016]) would live long enough to propagate far into the eastern subdomain (box E), but their number and thus relative contribution is expected to be small.

A simple box model of the surface mixed layer was used to estimate the role of eddies in maintaining a steady state distribution of salinity in the subtropical North Atlantic. The eddy salt flux divergence (equation

(4)) in the SSS maximum area was computed with two different approaches, concluding that eddies can compensate between 4% and 21% of the annual excess of evaporation over precipitation (between 6 and 29% if the variability of the MLD is not taken into account). Our estimates contrast with the values given by *Gordon and Giulivi* [2014]. They concluded that mesoscale eddies can supply up to 75% (depending on the MLD used) of the necessary freshwater convergence to compensate for the excess of evaporation over precipitation in the SSS maximum area. They used data recovered from a hydrographic section crossing the salinity maximum and outputs of a model (SODA reanalysis) for their estimations. One of the reasons for this discrepancy could be in the different definition of the eddy field. While we considered only coherent features detected in SLA fields, *Gordon and Giulivi* [2014] defined eddy salinity and temperature anomalies as deviations from the section mean, which could overestimate the intensity of the anomalies since it could include multiscale ocean turbulence and other processes that can generate additional fluxes. In our study, we use a more narrow definition of the eddy field and consider only large, long-lived mesoscale eddies observed by the satellites. However, there is a large and growing body of evidence suggesting that the horizontal eddy heat and salt fluxes in the ocean are primarily due to large mesoscale eddies. This would be consistent with theoretical arguments [*Larichev and Held*, 1995; *Thompson and Young*, 2007] and also supported by observations and modelling studies. For example, numerical experiment by *Capet et al*. [2008] demonstrate that unlike vertical eddy fluxes, the horizontal eddy fluxes are dominated by contributions from large mesoscale eddies and change only modestly under increasing resolution. *Abernathey and Wortham* [2015] investigated spectral characteristics of the eddy heat fluxes near the ocean surface from

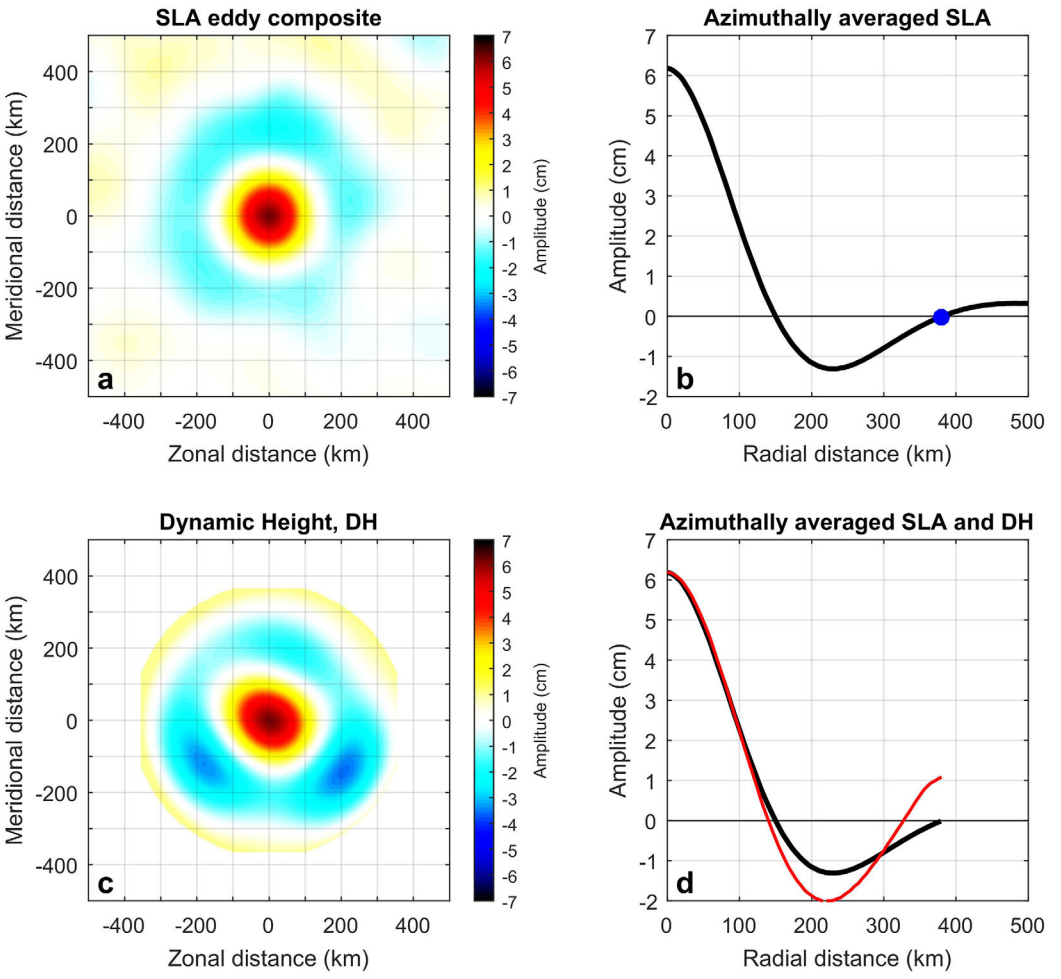

Figure 10. (a) Average composite map of SLA for anticyclonic eddies identified in the northern subregion (box N in Figure 2a)). (b) Composite profile of eddy SLA (black) as a function of radius. Blue dot shows the second zero crossing, marking the maximum radius used for computing the eddy composites (section 3.3). (c) Resulting dynamic height from the eddy composite salinity and temperature anomalies. (d) Comparison between the SLA radial profile (black) and the dynamic height profile (red).

concurrent satellite SLA and SST data and found that the dominant length scales for the heat fluxes were very close to the scales of the mesoscale eddies identified by *Chelton et al*. [2011]. These arguments make our analysis of eddy composites very relevant. Our estimates of the eddy salt fluxes from observations of mesoscale eddies are also in line with the modelling study by *Tréguier et al*. [2012]. They estimated that the eddy salt transport divergence across the subtropical gyre is significant and can account for as much as 30% of the evaporation-precipitation balance over the area. These estimates are also consistent with a recent modelling study by *Busecke et al*. [2016], who conclude that mesoscale eddies play a significant role in the mean surface freshwater balance in the subtropical North Atlantic providing about 20% contribution. The remaining effect of the E-P flux on the ML salinity, not explained by the eddy salt divergence, must be compensated, in a steady balance, by other ocean processes. Among them, the most important process is the seasonal Ekman advection followed by vertical mixing and entrainment [*Yu*, 2011].

Appendix A: Sea Level Anomaly Composite Analysis and Determination of the Reconstruction Domain

For the eddy composite analysis, weekly fields of SLA were sampled in 500 km by 500 km boxes centered on each eddy identified in the eddy data set [*Chelton et al*., 2011]. The composite averaging was then performed over all boxes. For each subregion identified in Figure 2a, the eddy composites included only eddies located inside the areas' geographic bounds. An example for the northern subregion, anticyclonic eddy, is presented in Figure 10a. As expected [*Chelton et al*., 2011], the composite eddy has a bell-like shape across the eddy interior with little or no sign of anisotropy. The amplitude of the composite eddy in SLA is determined as the extremum at the eddy center (6.2 cm in this particular case). The average eddy profile (black curve in Figure 10b) is used to determine the outer boundary of the reconstruction domain, L, selected as the second zero crossing (blue dot Figure 10b). The dynamic height anomaly of the composite eddy (Figures 10c and 10d) reconstructed with the procedure detailed in section 3.3 is in good agreement with the SLA eddy composite obtained from the satellite images (Figures 10a and 10b).

Appendix B: Robustness Estimation

The sources of errors in the eddy composite analysis are diverse. These include, but are not limited to, potential errors in the automated eddy detection and identification [*Chelton et al*., 2011], uncertainties in the positioning of Argo profiles, instrument errors in temperature/salinity measurements along the profiles, contamination from internal waves, and other fine-scale processes, among others. Characterization and quantification of all these errors is a difficult task and beyond the scope of the present study. However, the robustness of the eddy composites and the associated flux estimates (Figure 7) were evaluated in the following manner. For each eddy composite, 150 subsets of the Argo profile data (section 2.3) were generated by discarding 50% of profiles, chosen randomly. For each subset of the data, the eddy composite and the associated fluxes were computed following the procedures outlined in sections 2.3 and 3.3.2. A standard deviation from the average over all such experiments was used to compute confidence intervals in Figure 7. The shaded area around each curve in Figure 7 corresponds to one standard deviation computed from those 150 realizations. As seen in Figure 7, the standard deviation intervals are relatively small, indicating that our eddy flux estimates are robust with respect to errors and uncertainties in the data.

Acknowledgments
This research was supported by the National Aeronautic and Space Administration (NASA) Physical Oceanography Program through grant NNX13AM86G. Additional support was provided by the Japan Agency for Marine-Earth Science and Technology (JAMSTEC), by NASA through grant NNX07AG53G, and by the National Oceanic and Atmospheric Administration (NOAA) through grant NA17RJ1230 through their sponsorship of research activities at the International Pacific Research Center. Argo data were collected and made freely available by the International Argo Program and the national programs that contribute to it (http://www.argo.ucsd.edu). We want to thank the global ocean heat flux and evaporation products provided by the WHOI OAFlux project (http://oaflux.whoi.edu) funded by the NOAA Climate Observations and Monitoring (COM) program and also the World Climate Research Program (WCRP) and the Global Energy and Water Exchange program (GEWEX) for the precipitation data set computed in the Global Precipitation Climatology Project (GPCP). We are thankful to Dudley Chelton for the eddy data set (downloaded from http://cioss.coas.oregonstate.edu/eddies/nc_data.html) and M. Izumi for editing the manuscript. A. Amores is grateful to S. Monserrat and C. Blázquez for their help during the preparation of this paper. Comments and suggestions by two anonymous reviewers helped improve the quality of the manuscript. This paper is IPRC/SOEST contribution 1231/9883.

References

Abernathey, R., and C. Wortham (2015), Phase speed cross spectra of eddy heat fluxes in the Eastern Pacific, *J. Phys. Oceanogr.*, *45*(5), 1285–1301, doi:10.1175/JPO-D-14-0160.1.

Adler, R. F., et al. (2003), The version-2 global precipitation climatology project (GPCP) monthly precipitation analysis (1979-present), *J. Hydrometeorol.*, *4*(6), 1147–1167, doi:10.1175/1525-7541(2003)004 < 1147:TVGPCP>2.0.CO;2.

Amores, A., S. Monserrat, and M. Marcos (2013), Vertical structure and temporal evolution of an anticyclonic eddy in the Balearic Sea (western Mediterranean), *J. Geophys. Res. Oceans*, *118*, 2097–2106, doi:10.1002/jgrc.20150.

AVISO (2015), *SSALTO/DUACS User Handbook*: *(M)SLA and (M)ADT Near-Real Time and Delayed Time Products*, CLS-DOS-NT-06-034, Issue 4.4. [Available at http://www.aviso.altimetry.fr/fileadmin/documents/data/tools/hdbk_duacs.pdf.]

Bennett, A. F., and W. B. White (1986), Eddy heat flux in the subtropical North Pacific, *J. Phys. Oceanogr.*, *16*(4), 728–740, doi:10.1175/1520-0485(1986)016 < 0728:EHFITS>2.0.CO;2.

Busecke, J., R. Abernathey, and A. L. Gordon (2016), Eddy mixing in the subtropical surface salinity maximum regions, Abstract PO31B-08 presented at *Ocean Sciences Meeting organized by the American Geophysical Union (AGU),* New Orleans. [Available at https://agu.confex.com/agu/os16/meetingapp.cgi/Paper/88985.]

Capet, X., J. C. McWilliams, M. J. Molemaker, and A. F. Shchepetkin (2008), Mesoscale to Submesoscale Transition in the California Current System. Part I: Flow Structure, Eddy Flux, and Observational Tests, *J. Phys. Oceanogr.*, *38*(1), 29–43, doi:10.1175/2007JPO3671.1.

Castelao, R. M. (2014), Mesoscale eddies in the South Atlantic Bight and the Gulf Stream recirculation region: Vertical structure, *J. Geophys. Res. Oceans*, *119*, 2048–2065, doi:10.1002/2014JC009796.

Chaigneau, A., M. Le Texier, G. Eldin, C. Grados, and O. Pizarro (2011), Vertical structure of mesoscale eddies in the eastern South Pacific Ocean: A composite analysis from altimetry and Argo profiling floats, *J. Geophys. Res. Oceans*, *116*, C11025, doi:10.1029/2011JC007134.

Chelton, D. B., M. G. Schlax, R. M. Samelson, and R. A. de Szoeke (2007), Global observations of large oceanic eddies, *Geophys. Res. Lett.*, *34*, L15606, doi:10.1029/2007GL030812.

Chelton, D. B., M. G. Schlax, and R. M. Samelson (2011), Global observations of nonlinear mesoscale eddies, *Prog. Oceanogr.*, *91*(2), 167–216, doi:10.1016/j.pocean.2011.01.002.

Early, J. J., R. Samelson, and D. B. Chelton (2011), The evolution and propagation of quasigeostrophic ocean eddies*, *J. Phys. Oceanogr.*, *41*(8), 1535–1555, doi:10.1175/2011JPO4601.1.

Emery, W., and J. Meincke (1986), Global water masses: Summary and review, *Oceanol. Acta*, *9*, 383–391.

Faghmous, J. H., I. Frenger, Y. Yao, R. Warmka, A. Lindell, and V. Kumar (2015), A daily global mesoscale ocean eddy dataset from satellite altimetry, *Sci. Data*, *2*, doi:10.1038/sdata.2015.28. [Available at http://www.nature.com/articles/sdata201528.]

Farrar, J. T., et al. (2015), Salinity and temperature balances at the SPURS Central mooring during fall and winter, *Oceanography*, *28*, 56–65, doi:10.5670/oceanog.2015.06.

Flierl, G. R. (1981), Particle motions in large-amplitude wave fields, *Geophys. Astrophys. Fluid Dyn.*, *18*(1-2), 39–74, doi:10.1080/03091928108208773.

Frenger, I., M. Münnich, N. Gruber, and R. Knutti (2015), Southern Ocean eddy phenomenology, *J. Geophys. Res. Oceans*, *120*, 7413–7449, doi:10.1002/2015JC011047.

Gaube, P., D. B. Chelton, R. M. Samelson, M. G. Schlax, and L. W. ONeill (2015), Satellite observations of mesoscale eddy-induced Ekman pumping, *J. Phys. Oceanogr.*, *45*(1), 104–132, doi:10.1175/JPO-D-14-0032.1.

Gill, A. (1982), *Atmosphere Ocean Dynamics*, vol. 30, 662 pp., Academic Press, London and Calif. [Available at https://books.google.com/books?hl=en&lr=&id=8kFPh_SvnAIC&oi=fnd&pg=PP1&dq=Gill,+A.+(1982),+Atmosphere+Ocean+Dynamics,+vol.+30,+662p+pp.,+Academic.&ots=B86M6u2Uio&sig=KGWskh6QyhQt9qFZb4CO4LQic0M#v=onepage&q&f=false.]

Gill, A., J. Green, and A. Simmons (1974), Energy partition in the large-scale ocean circulation and the production of mid-ocean eddies, in *Deep Sea Research and Oceanographic Abstracts*, vol. 21, pp. 499–528, doi:10.1016/0011-7471(74)90010-2. [Available at http://www.sciencedirect.com/science/article/pii/0011747174900102.]

Good, S., M. Martin, and N. Rayner (2013), EN4: Quality controlled ocean temperature and salinity profiles and monthly objective analyses with uncertainty estimates, *J. Geophys. Res. Oceans*, *118*, 6704–6716, doi:10.1002/2013JC009067.

Gordon, A. L., and C. F. Giulivi (2014), Ocean eddy freshwater flux convergence into the North Atlantic subtropics, *J. Geophys. Res. Oceans*, *119*, 3327–3335, doi:10.1002/2013JC009596.

Hanawa, K., and L. D. Talley (2001), Mode waters, *Int. Geophys. Ser.*, *77*, 373–386.

Hausmann, U., and A. Czaja (2012), The observed signature of mesoscale eddies in sea surface temperature and the associated heat transport, *Deep Sea Res., Part I*, *70*, 60–72, doi:10.1016/j.dsr.2012.08.005.

Holte, J., J. Gilson, L. Talley, and D. Roemmich (2010), *Argo Mixed Layers*, Scripps Inst. of Oceanogr./UCSD. [Available at http://mixedlayer.ucsd.edu, Accessed May 2015.]

Huffman, G. J., R. F. Adler, D. T. Bolvin, and G. Gu (2009), Improving the global precipitation record: GPCP version 2.1, *Geophys. Res. Lett.*, *36*, L17808, doi:10.1029/2009GL040000.

Jayne, S. R., and J. Marotzke (2002), The oceanic eddy heat transport*, *J. Phys. Oceanogr.*, *32*(12), 3328–3345, doi:10.1175/1520-0485(2002)032 < 3328:TOEHT>2.0.CO;2.

Larichev, V. D., and I. M. Held (1995), Eddy amplitudes and fluxes in a homogeneous model of fully developed baroclinic instability, *J. Phys. Oceanogr.*, *25*(10), 2285–2297, doi:10.1175/1520-0485(1995)025 < 2285:EAAFIA>2.0.CO;2.

Laurian, A., A. Lazar, and G. Reverdin (2009), Generation mechanism of spiciness anomalies: An OGCM analysis in the north Atlantic subtropical gyre, *J. Phys. Oceanogr.*, *39*(4), 1003–1018, doi:10.1175/2008JPO3896.1.

Marshall, J., H. Jones, R. Karsten, and R. Wardle (2002), Can eddies set ocean stratification?, *J. Phys. Oceanogr.*, *32*(1), 26–38, doi:10.1175/1520-0485(2002)032 < 0026:CESOS>2.0.CO;2.

Mason, E., A. Pascual, and J. McWilliams (2014), A new sea surface height–based code for oceanic mesoscale eddy tracking, *J. Atmos. Oceanic Technol.*, *31*(5), 1181–1188.

Maximenko, N., P. Niiler, L. Centurioni, M.-H. Rio, O. Melnichenko, D. Chambers, V. Zlotnicki, and B. Galperin (2009), Mean dynamic topography of the ocean derived from satellite and drifting buoy data using three different techniques, *J. Atmos. Oceanic Technol.*, *26*(9), 1910–1919, doi:10.1175/2009JTECHO672.1.

Melzer, B. A., and B. Subrahmanyam (2015), Investigating decadal changes in sea surface salinity in oceanic subtropical gyres, *Geophys. Res. Lett.*, *42*, 7631–7638, doi:10.1002/2015GL065636.

Nencioli, F., C. Dong, T. Dickey, L. Washburn, and J. C. McWilliams (2010), A vector geometry-based eddy detection algorithm and its application to a high-resolution numerical model product and high-frequency radar surface velocities in the southern California bight, *J. Atmos. Oceanic Technol.*, *27*, 564–579, doi:10.1175/2009JTECHO725.1.

O'Connor, B. M., R. A. Fine, and D. B. Olson (2005), A global comparison of subtropical underwater formation rates, *Deep Sea Res., Part I*, *52*(9), 1569–1590, doi:10.1016/j.dsr.2005.01.011.

Qiu, B., and S. Chen (2005), Variability of the Kuroshio Extension jet, recirculation gyre, and mesoscale eddies on decadal time scales, *J. Phys. Oceanogr.*, *35*(11), 2090–2103, doi:10.1175/JPO2807.1.

Qu, T., S. Gao, and I. Fukumori (2013), Formation of salinity maximum water and its contribution to the overturning circulation in the North Atlantic as revealed by a global general circulation model, *J. Geophys. Res. Oceans*, *118*, 1982–1994, doi:10.1002/jgrc.20152.

Roemmich, D., and J. Gilson (2001), Eddy transport of heat and thermocline waters in the North Pacific: A key to interannual/decadal climate variability?, *J. Phys. Oceanogr.*, *31*(3), 675–687, doi:10.1175/1520-0485(2001)031 < 0675:ETOHAT>2.0.CO;2.

Schmitt, R. W., and A. Blair (2015), A River of Salt, *Oceanography*, *28*(1), 40–45, doi:10.5670/oceanog.2015.04. [Available at http://dx.doi.org/10.5670/oceanog.2015.04.]

Schott, F. A., J. P. Mccreary, and G. C. Johnson (2004), *Shallow Overturning Circulations of the Tropical-Subtropical Oceans*, pp. 261–304, American Geophysical Union, doi:10.1029/147GM15. [Available at http://onlinelibrary.wiley.com/doi/10.1029/147GM15/summary.]

Schütte, F., P. Brandt, and J. Karstensen (2016), Occurrence and characteristics of mesoscale eddies in the tropical northeastern Atlantic Ocean, *Ocean Sci.*, *12*(3), 663–685, doi:10.5194/os-12-663-2016.

Souza, J., C. de Boyer Montégut, C. Cabanes, and P. Klein (2011), Estimation of the Agulhas ring impacts on meridional heat fluxes and transport using ARGO floats and satellite data, *Geophys. Res. Lett.*, *38*, L21602, doi:10.1029/2011GL049359.

Spall, M. A. (2000), Generation of strong mesoscale eddies by weak ocean gyres, *J. Marine Res.*, *58*(1), 97–116, doi:10.1357/002224000321511214.

Stammer, D. (1998), On eddy characteristics, eddy transports, and mean flow properties, *J. Phys. Oceanogr.*, *28*(4), 727–739, doi:10.1175/1520-0485(1998)028 < 0727:OECETA>2.0.CO;2.

Sverdrup, H. U. (1947), Wind-driven currents in a baroclinic ocean; with application to the equatorial currents of the eastern Pacific, *Proc. Natl. Acad. Sci. U. S. A.*, *33*(11), 318–326.

Talley, L. D. (2002), Salinity patterns in the ocean, in *Encyclopedia of Global Change. Volume: The Earth System: Physical and Chemical Dimensions of Global Environmental*, edited by Change, M. C. MacCracken and J. S. Perry, pp. 629–640, John Wiley & Sons, Ltd, Chichester. [Available at https://pdfs.semanticscholar.org/213c/ca4e6779f67bae064f2f90981540b643a27b.pdf.]

Thompson, A. F., and W. R. Young (2006), Scaling baroclinic eddy fluxes: Vortices and energy balance, *J. Phys. Oceanogr.*, *36*(4), 720–738, doi:10.1175/JPO2874.1.

Thompson, A. F., and W. R. Young (2007), Two-layer baroclinic eddy heat fluxes: Zonal flows and energy balance, *J. Atmos. Sci.*, *64*(9), 3214–3231, doi:10.1175/JAS4000.1.

Tréguier, A.-M., J. Deshayes, C. Lique, R. Dussin, and J.-M. Molines (2012), Eddy contributions to the meridional transport of salt in the North Atlantic, *J. Geophys. Res. 117*, C05010, doi:10.1029/2012JC007927.

Tréguier, A.-M., J. Deshayes, J. Le Sommer, C. Lique, G. Madec, T. Penduff, J.-M. Molines, B. Barnier, R. Bourdalle-Badie, and C. Talandier (2014), Meridional transport of salt in the global ocean from an eddy-resolving model, *Ocean Sci.*, *10*(2), 243–255, doi:10.5194/os-10-243-2014.

Wang, Q., O. Ronneberger, and H. Burkhardt (2008), Fourier analysis in polar and spherical coordinates, Albert-Ludwigs-Univ. Freiburg, Inst. für Informatik, Technical Report Internal Report 1/08, IIF-LMB, Computer Science Department, University of Freiburg. [Available at http://lmb.informatik.uni-freiburg.de/Publications/2008/WRB08/.]

Wunsch, C. (1999), Where do ocean eddy heat fluxes matter?, *J. Geophys. Res.*, *104*, 13,235–13,249.

Yu, L. (2007), Global variations in oceanic evaporation (1958-2005): The role of the changing wind speed, *J. Clim.*, *20*(21), 5376–5390, doi:10.1175/2007JCLI1714.1.

Yu, L., X. Jin, and R. A. Weller (2008), Multidecade Global Flux Datasets from the Objectively Analyzed Air-sea Fluxes (OAFlux) Project: Latent and sensible heat fluxes, ocean evaporation, and related surface meteorological variables, *Tech. Rep. OA-2008-01*, 64 pp., Woods Hole Oceanogr. Inst., OAFlux Proj., Woods Hole. Mass.

Yu, L. (2011), A global relationship between the ocean water cycle and near-surface salinity, *J. Geophys. Res.*, *116*, C10025, doi:10.1029/2010JC006937.